

Patch Triplet Similarity Purification for Guided Real-World Low-Dose CT Image Denoising

Junhao Long, Fengwei Yang, Juncheng Yan, Baoping Zhang, Chao Jin, Jian Yang, Changliang Zou, Jun Xu

Abstract—Image denoising of low-dose computed tomography (LDCT) is an important problem for clinical diagnosis with reduced radiation exposure. Previous methods are mostly trained with pairs of synthetic or misaligned LDCT and normal-dose CT (NDCT) images. However, trained with synthetic noise or misaligned LDCT/NDCT image pairs, the denoising networks would suffer from blurry structure or motion artifacts. Since non-contrast CT (NCCT) images share the content characteristics to the corresponding NDCT images in a three-phase scan, they can potentially provide useful information for real-world LDCT image denoising. To exploit this aspect, in this paper, we propose to incorporate clean NCCT images as useful guidance for the learning of real-world LDCT image denoising networks. To alleviate the issue of spatial misalignment in training data, we design a new Patch Triplet Similarity Purification (PTSP) strategy to select highly similar patch (instead of image) triplets of LDCT, NDCT, and NCCT images for network training. Furthermore, we modify two image denoising transformers of SwinIR and HAT to accommodate the NCCT image guidance, by replacing vanilla self-attention with cross-attention. On our collected clinical dataset, the modified transformers trained with the data selected by our PTSP strategy show better performance than 15 comparison methods on real-world LDCT image denoising. Ablation studies validate the effectiveness of our NCCT image guidance and PTSP strategy. We will publicly release our data and code.

Index Terms—Low-dose CT image denoising, transformer, patch triplet similarity purification, cross-attention

I. INTRODUCTION

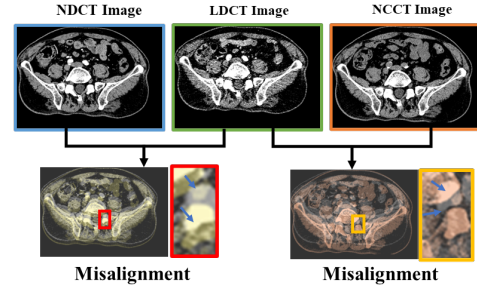
THE technology of computerized tomography (CT) scanning is widely used for clinical diagnosis [23], [33], [50]. For example, the annual frequency of CT examinations was 239.8 per 1000 inhabitants [26]. However, the exposure to radiation by X-rays in CT scanning brings potential health risks to the human body [48]. To alleviate this problem, it is essential to reduce the dose usage of CT scanning in clinical diagnosis. But low-dose CT (LDCT) images usually suffer from unclear details due to noise and artifacts, making it difficult for

This research is supported by The National Natural Science Foundation of China (No. 12226007, 62176068, and 62171309), the Open Research Fund from the Guangdong Provincial Key Laboratory of Big Data Computing, The Chinese University of Hong Kong, Shenzhen, under Grant No. B10120210117-OF03, Youth Project of Tianjin Municipal Applied Basic Research Project (23JCQNJC01630), and the Fundamental Research Funds for the Central Universities. Corresponding author: Jun Xu (csjunxu@nankai.edu.cn) and Juncheng Yan (yanjuncheng@mail.nankai.edu.cn)

J.-H. Long, F.-W. Yang, J.-C. Yan, C.-L. Zou, and J. Xu are with School of Statistics and Data Science, Nankai University, Tianjin, 300071, China.

B.-P. Zhang, J. Chao and J. Yang are with the Department of Radiology, The First Affiliated Hospital of Xi'an Jiaotong University, Xi'an, China; Shanxi Engineering Research Center of Computational Imaging and Medical Intelligence, Xi'an, China and Xi'an Key Laboratory of Medical Computational Imaging, Xi'an, China.

(a) Spatial misalignment among NDCT, LDCT and NCCT images



(b) Cropped patch triplets from NDCT, LDCT and NCCT images

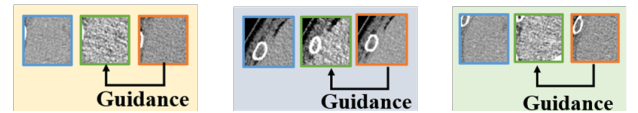


Figure 1. Motivation of our NCCT image guidance and Patch Triplet Similarity Purification (PTSP) strategy. (a) The NCCT image enjoys structural similarity with the corresponding NDCT images from three-phase scanning. However, when overlapping LDCT images with the corresponding NDCT and NCCT images, there exists clear spatial misalignment. (b) Utilizing patch-level guidance instead of image-level one for network training.

physicians to accurately diagnose lesions. Thus, LDCT image denoising becomes a meaningful research topic.

During the past decade, many LDCT image denoising methods have been developed based on deep convolutional neural networks (CNN) [9], [10], [30] or transformers [1], [36], [72]. These works mainly tackle synthetic LDCT images generated by adding Poisson noise to the sinogram data of the corresponding normal-dose CT (NDCT) images [9]. But the denoising networks trained with synthetic noise which is really different from the noise of the real-world LDCT images usually perform poorly in removing realistic noise [44], [60], [64]. To address real-world noise in clinical scenarios, several recent methods [2], [6], [34], [60] perform LDCT image denoising under self-supervised learning frameworks [22], [67]. However, without supervision of the NDCT images, it is still difficult to remove complex noise from the real-world LDCT images [9], [56], [62]. For real-world LDCT image denoising, many methods [3], [37], [65] employ generative adversarial networks (GAN) [17], [71] to learn direct mappings between real-world LDCT images and their spatially similar but misaligned NDCT counterparts (Fig. 1). However, using such “pairs” of LDCT and NDCT images for network training would result in structural distortions in the restored images.

In clinical practice, the non-contrast CT (NCCT) images

are usually scanned to provide vascularization characteristics and enhanced lesion patterns of the LDCT images. As shown in Fig. 1, for an LDCT image, its NCCT image has similar structure to its NDCT image. This indicates that NCCT images can provide helpful guidance on LDCT image denoising which is ignored by past researches. To exploit this aspect, in this paper, we propose to modify popular image denoising transformers [12], [40] to accommodate with “triplets” of LDCT, NDCT, and NCCT images. However, it is necessary to minimize the side effects of spatial misalignment among the LDCT, NDCT, and NCCT images (Fig. 1) on training real-world LDCT image denoising networks. For this goal, we propose a Patch Triplet Similarity Purification (PTSP) strategy to select highly similar NDCT and NCCT image patches as the “target” and guidance reference, respectively, of each LDCT image patch at the same locations of corresponding images. Our PTSP strategy is built upon pixel value discretization [52] to be robust on noise degradation in LDCT images.

With highly similar training data selected by our PTSP strategy, we employ cross-attention [8] to incorporate useful information from clean NCCT images into image denoising transformers for guided LDCT image denoising. Experiments on our synthetic and clinical datasets demonstrate that, with our NCCT guidance and PTSP strategy, the modified SwinIR [40] and HAT [12] obtain better LDCT image denoising performance than 15 comparison methods. Ablation studies validate the effectiveness of our NCCT image guidance and PTSP strategy in selecting high-quality training triplets of LDCT, NDCT, and NCCT image patches for LDCT image denoising.

In summary, our main contributions are three-fold:

- To exploit extra information from clean NCCT images, **we propose to incorporate NCCT image as useful guidance for real-world LDCT image denoising.** This is implemented by replacing vanilla self-attention with cross-attention in image denoising transformers.
- To address the spatial misalignment between real-world LDCT images and NDCT/NCCT images, **we propose a Patch Triplet Similarity Purification (PTSP) strategy to select highly similar triplets of LDCT, NDCT, and NCCT image patches with negligible misalignment as high-quality training data for LDCT image denoising.**
- **Incorporated by the guidance from NCCT images, two transformers [12], [40] modified to be trained using our PTSP strategy outperform fifteen LDCT image denoising methods** on our collected clinical dataset.

The remaining parts of this paper are organized as follows. We present the related work in §II. In §III, we propose our PTSP strategy and NCCT image guidance. In §IV, we provide the introduction of our synthetic dataset and clinical dataset. Experiments in §V demonstrated that our PTSP strategy and NCCT image guidance boosts two LDCT denoising networks both quantitatively and qualitatively. The conclusion is summarized in §VI.

II. RELATED WORK

In this section, we introduce the work closely related to ours, including the LDCT image denoising methods in §II-A,

self-supervised image denoising method in §II-B, and guided image denoising in §II-C.

A. Low-Dose CT Image Denoising

Low-dose CT (LDCT) image denoising is initially tackled with first convolutional neural networks (CNNs) [10]. The RED-CNN network [9] was developed with an encoder-decoder architecture for favorable performance. Kang *et al.* [30], [32] proposed to learn wavelet transforms with CNNs for LDCT image denoising. Compared to CNNs [41], transformers [58] are good at capturing global information and long-range feature interactions, which have been applied to LDCT image denoising for better performance [56]. Vision Transformer (ViT) [1] has also been utilized in [56], [57] to enlarge the effective receptive fields of window-based transformers for better denoising performance. Li *et al.* [36] devised a dual-branch transformer to recover the edges and textures of LDCT images well. However, the above methods are trained with synthetic LDCT images and could hardly be applied to real-world LDCT images in clinical practice.

For clinical purposes, researchers proposed to learn mapping from real-world LDCT images to high-quality NDCT ones using the GAN architectures [17]. Wolterink *et al.* [59] trained a CNN jointly with an adversarial CNN to recover the NDCT images from LDCT images. Yi and Babyn [66] trained an adversarial network together with a sharpness detection network to mitigate the blurring effects in LDCT image denoising. Later, many LDCT image denoising methods are built upon CycleGAN [31], [54], conditional GAN [21], or WGAN [25], [65]. However, the structural misalignment between real-world LDCT images and NDCT images makes it difficult to guarantee the fidelity of denoised images [35].

In this paper, we also use real-world LDCT images to train the denoising networks, thereby well serving clinical practice. To alleviate the problem of image structure misalignment between LDCT and NDCT images, we propose a Patch Triplet Similarity Purification (PTSP) strategy to select highly-similar patch triplets for training LDCT image denoising networks.

B. Self-Supervised Image Denoising

Self-supervised image denoising methods [6], [60] learn from the noisy images themselves to remove the noise without using clean images. By assuming that noise is zero-mean and independently and identically distributed (i.i.d.), Noise2Noise (N2N) [6] effectively trains image denoising using pairs of noisy images with the same contents but different noise. Noise2Void (N2V) [34] learns to predict the true value of each noisy pixel from its neighboring pixels, and hence called “blind-spot” method. Unlike N2V, Noise2Self (N2S) [2] additionally performs masking operations for each pixel to enhance the denoising robustness. Noise-As-Clean (NAC) [60] learns to remove image noise with a pair of noisy image and noisier image, which is produced by adding synthetic noise to the noisy image. However, the above-mentioned denoising methods mainly learn to remove the zero-mean and i.i.d. noise, which may not hold true for real-world LDCT images.

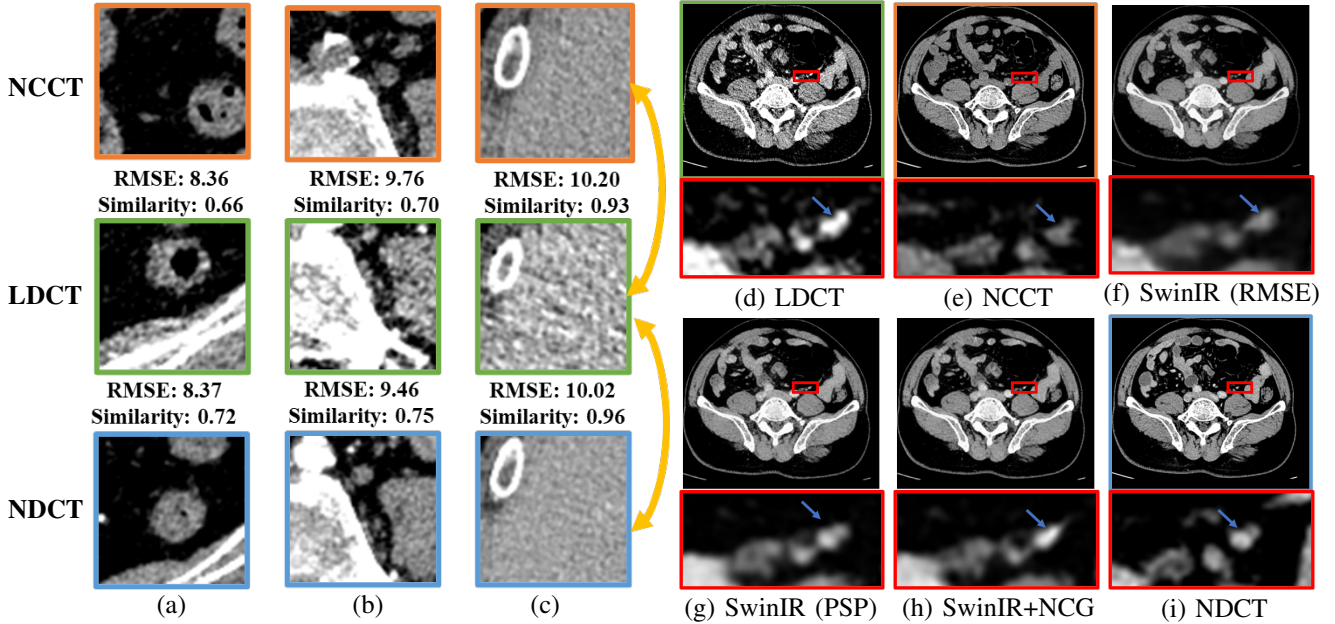


Figure 2. **Training data screening strategy based on RMSE vs. our Patch Triplet Similarity Purification (PTSP) strategy.** Mask Similarity is abbreviated as “Similarity”. Subfigure (a) shows more significant structure differences among LDCT, NDCT, and NCCT image patches than (b) and (c). However, the RMSE metric gives the opposite conclusion. There are obvious “brightness” differences among the three image patches in (c). The average pixel value of the LDCT patch is 169.23, which is 25.26 higher than the average pixel value of the NCCT patch and 10.64 higher than that of the NDCT patch. (d) An LDCT image. (e) The corresponding NCCT image. (f) The denoised image of SwinIR [40] trained with the data screened by the RMSE metric (g) The denoised image of SwinIR by introducing PSP strategy [52]. (h) The denoised image of SwinIR by introducing NCCT image guidance and our PTSP strategy. (i) The corresponding NDCT image. In general, the proposed NCCT image guidance and PTSP strategy for training data selection well recover the structure of the denoised image on real-world LDCT image denoising.

Self-supervised learning has also been applied to LDCT image denoising by only using LDCT images. Noise2Inverse [19] performs image reconstruction [45] by learning a CNN without additional clean or noisy data. Noise2Sim [47] is a self-supervised deep denoising approach that achieves noise reduction by using similar images. However, because of the lack of supervision from high-quality NDCT images, it is challenging for these self-supervised denoisers to remove complex noise well in real-world LDCT images.

In this paper, we propose to train denoising networks with pairs of highly similar LDCT and NDCT image patches selected by our similarity purification strategy.

C. Guided Image Denoising

Many image denoising methods utilize useful spatial or edge information from external clean images for guided image denoising. He *et al.* [18] proposed guided image filtering (GIF) to use the guidance image to identify noise and edges for better noise reduction. Based on GIF, the method of [39] incorporates an edge-aware weighting strategy for edge-preserving image filtering. Xu *et al.* [63] exploited the external information from clean images to guide the internal learning of a noisy test image for real-world image denoising. Zhang *et al.* [69] utilized the mean image of all spectral bands as useful guidance to adaptively aggregate spatial information.

The insights of external guidance also boost LDCT image denoising. For example, edge-guided filtering [14] and GDAFormer [27] use edge feature to guide the learning of LDCT image denoising. In this paper, we use Non-Contrast CT (NCCT) image to guide the LDCT image denoising.

III. PROPOSED METHOD

In this section, we propose a NCCT image guidance for LDCT image denoising in §III-A. Then we introduce our Patch Triplet Similarity Purification (PTSP) strategy in §III-B, to select highly similar training data. With our PTSP strategy, we integrate the guidance of NCCT images into two denoising Transformers for LDCT image denoising in §III-C.

A. NCCT-Guided LDCT Image Denoising

For LDCT image denoising, the self-attention-based transformers [27] achieve promising performance when trained with LDCT and NDCT images. However, this may inaccurately estimate the tissue structure of LDCT images with noise degradation. What’s more, these methods ignored the useful information from the NCCT images, which are widely used for preliminary diagnosis of diseases in clinical practice [55]. As shown in Fig. 1, the NCCT image has similar structure and texture to the corresponding NDCT image, which provides useful information for LDCT image denoising. Inspired by this observation, we propose to utilize the clean NCCT images as complementary guidance to remove the noise from LDCT images. This guidance can be implemented in a cross-attention mechanism [8] for transformer based denoisers [12], [40], where the LDCT image provides the query matrix Q and value matrix V while the NCCT image provides the key matrix K . This allows cross-attention to establish the associations between the noisy LDCT image and the corresponding clean NCCT image, enhancing the capability of the denoising transformers on structure preserving and texture recovery.

Direct using triplets of LDCT, NDCT, and NCCT images for network training does not bring promising performance

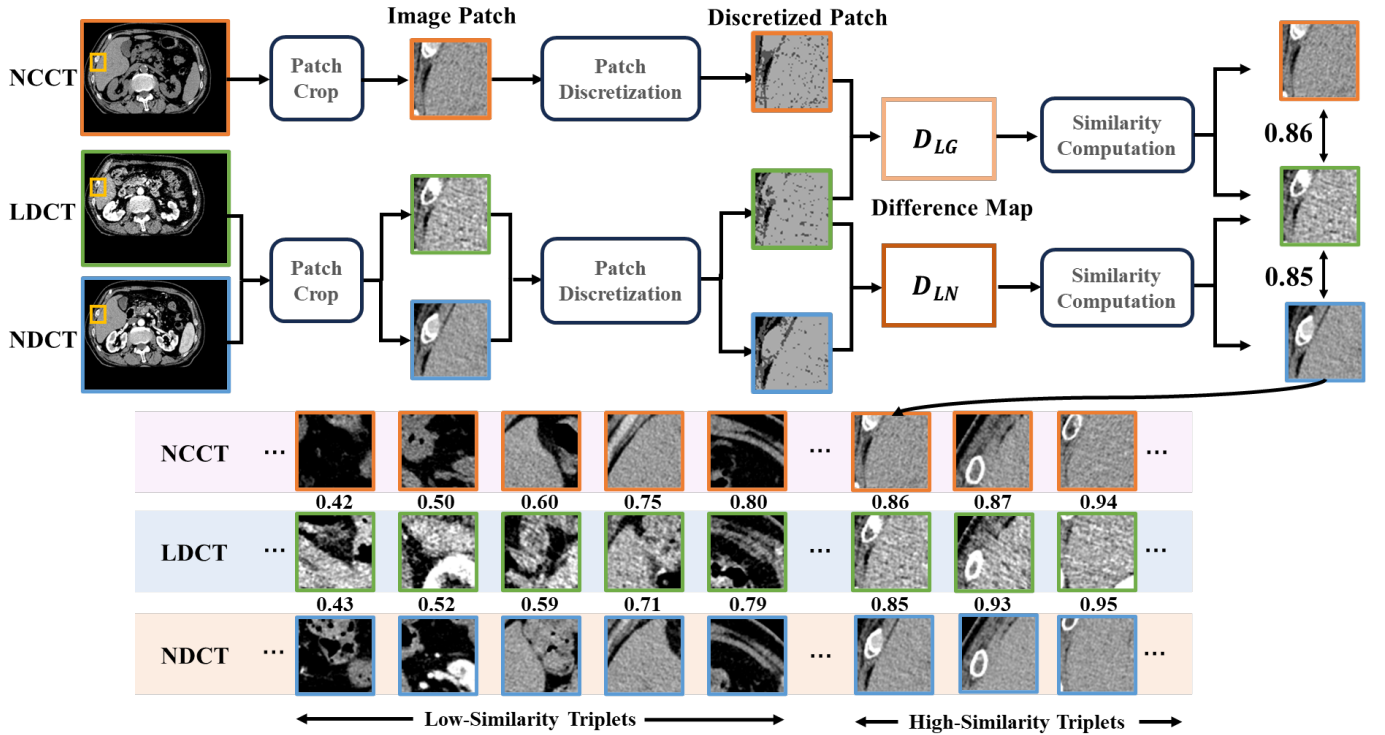


Figure 3. **The proposed Patch Triplet Similarity Purification (PTSP) Strategy.** It includes three main steps: 1) compute the discretized image patches M_G , M_L , and M_N according to the set pixel interval; 2) obtain the difference maps D_{LN} (or D_{LG}) by subtracting the discretized LDCT image patch from the discretized NDCT (or NCCT) image patch; 3) compute the corresponding mask similarity based on difference maps. When the mask similarity reaches a preset threshold s (e.g., $s = 0.85$), we include it in the training set of our clinical dataset.

on LDCT image denoising. The key problem is that the images from the three-phase scanning suffer from clear spatial misalignment (Fig. 1). To alleviate this issue, we propose to select highly similar patch triplets (instead of image triplets) for network training, as will be introduced as follows.

B. Proposed Patch Triplet Similarity Purification Strategy

To address spatial misalignment between LDCT and NDCT images, a natural idea is to select pairs of highly similar LDCT and NDCT images for network training. Similarity can be measured using the RMSE metric [5], [13], [61], [70]. That is, for each reference LDCT patch, these methods search for the most similar patch to it from the NDCT image as the training “target”. However, the RMSE metric is error-prone in measuring the similarity between LDCT and NDCT image patches, since the distance is largely influenced by the noise in LDCT images and the misalignment between LDCT and NDCT images (Fig. 2). For example, the patches in Fig. 2 (c) are more similar to each other from the perspective of visual effects than those in Fig. 2 (a) and (b). However, the RMSE distances could not reflect this trend. Training transformers using pairs of similar LDCT and NDCT patches selected by minimal RMSE distance would result in vague structure or visual distortions in the denoised images like Fig. 2 (f). In contrast, transformers trained with the introduction of NCCT image guidance and our PTSP strategy effectively alleviate this issue, as shown in Fig. 2 (h).

To provide high-quality training data for guided LDCT image denoising, in this work, we propose a Patch Triplet Similarity

Purification (PTSP) strategy to select highly similar patch triplets from clinical LDCT, NDCT, and NCCT images with consistent tissue structures, which is shown in fig. 3. For each patch triplet, our PTSP strategy contains three main steps: 1) discretizing image patches according to the pixel intervals; 2) obtaining difference maps by subtracting the discretized LDCT patch from the discretized NDCT patch or NCCT patch; 3) computing the corresponding mask similarity based on the difference maps and obtaining the training patch triplets with high similarity.

Patch discretization. This step aims to describe the tissue content of each patch for similarity computation. The description of tissue contents is implemented by discretizing the pixel values of LDCT image patch, NDCT image patch, and NCCT image patch into multiple segments. Specifically, the pixel values in each CT image patch are between 0 and 255, we divide them into multiple segments separated by a set of predefined points $\{T_i\}_{i=0}^n$ that satisfies: $0 = T_0 < T_1 < \dots < T_n = 256$, where n is the number of segments. Denoting x as the position in LDCT patch p_L , NDCT patch p_N , or NCCT patch p_G of size $p \times p$ ($p = 64$ in our experiments), the discretized patch M_b (b is “L”, “N” or “G”) is defined as:

$$M_b(x) = \begin{cases} 0, & \text{if } T_0 \leq p_b(x) < T_1, \\ i - 1, & \text{if } T_{i-1} \leq p_b(x) < T_i, 1 < i < n, \\ n - 1, & \text{if } T_{n-1} \leq p_b(x) < T_n. \end{cases} \quad (1)$$

The set of separation points $\{T_i\}_{i=0}^n$ and the segment number n need to be predefined in advance. For example, when $n = 3$, $\{T_i\}_{i=0}^n$ can be set as $\{0, 85, 170, 256\}$ based on a linear

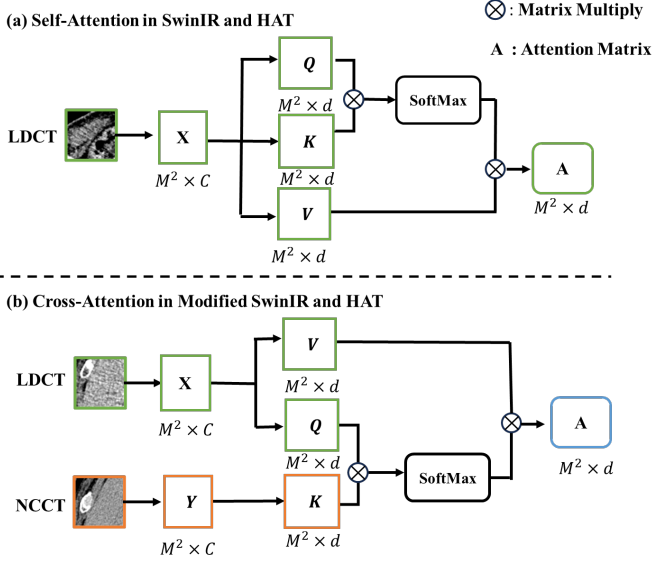


Figure 4. Architectures of Self-Attention (SA) in vanilla SwinIR/HAT and Cross-Attention (CA) in modified SwinIR/HAT to incorporate the guidance of NCCT images.

separation scheme. The separation points and the number of segments can be flexibly set based on the actual situation.

Patch differentiation. The goal of this step is to measure the distance between pairs of LDCT and NDCT image patches as well as between pairs of LDCT and NCCT image patches. In this step, the difference map D_{LN} (or D_{LG}) is obtained by subtracting the discretized NDCT patch M_N (or NCCT patch M_G) from the discretized LDCT patch M_L , as follows:

$$\begin{aligned} D_{LN}(x) &= |M_L(x) - M_N(x)|, \\ D_{LG}(x) &= |M_L(x) - M_G(x)|. \end{aligned} \quad (2)$$

The range of difference maps D_{LN} and D_{LG} is $0 \sim n-1$. Higher values at the position x of difference map D_{LN} (or D_{LG}) usually indicates larger difference between the corresponding pixel values of LDCT and NDCT (or NCCT) image patches at that pixel position x .

Similarity computation. To select highly-similar triplets of image patches for network training, it is essential to measure the similarity between LDCT and NDCT patches as well as LDCT and NCCT patches in our PTSP strategy. The greater difference in pixel values between patches at a position should indicate lower similarity at that position. To this end, we utilize a set of weights $\{\pi_i\}_{i=0}^{n-1}$ to satisfy $0 = \pi_{n-1} < \pi_{n-2} < \dots < \pi_0 = 1$. For example, when $n=3$, we can define $\{\pi_0 = 1, \pi_1 = 0.7, \pi_2 = 0\}$ to describe the differences in three levels. Denoting S_{LN} as the similarity mask to be computed, we assign different weights to different values of $D_{LN}(x)$ and compute the similarity mask S_{LN} as follows:

$$S_{LN}(x) = \begin{cases} \pi_0, & \text{if } D_{LN}(x) = 0, \\ \pi_j, & \text{if } D_{LN}(x) = j, 0 < j < n-1, \\ \pi_{n-1}, & \text{if } D_{LN}(x) = n-1. \end{cases} \quad (3)$$

The similarity mask S_{LG} can be similarly defined. Then we compute the proportion of the sum of non-zero values in S_{LN}

(or S_{LG}) to the total number of pixels (*i.e.*, p^2) in one LDCT image patch, as the mask similarity between LDCT and NDCT (or NCCT) image patches.

Selection of training patch triplets. Here, the NCCT images are used to provide structural guidance for real-world LDCT image denoising. However, the structural misalignment between LDCT and NDCT images is inconsistent as that between LDCT and NCCT images. Therefore, when the similarity between LDCT and NDCT image patches reaches a preset threshold $s \in (0, 1)$, we further search the surrounding area of the corresponding NCCT image patch to find the NCCT patch with the highest similarity to the LDCT patch. If the similarity between the LDCT and the NDCT image patch, as well as between the LDCT and the NCCT image patch, both exceed s , we will include this patch triplet into the training dataset. The threshold is set as $s = 0.85$ in our experiments and can be adjusted flexibly based on the actual dataset.

With highly similar ‘‘triplets’’ of LDCT, NDCT, and NCCT image patches, we modify and train the denoising transformers with the supervision of NDCT images and the guidance of NCCT images. In our PTSP strategy, we set the threshold of mask similarity as $s = 0.85$, which performs best in our ablation studies (§V-D). To study the effectiveness of our PTSP strategy, we also construct a training dataset using ‘‘pairs’’ of LDCT and NDCT images. Here, we only need to compare the similarity between LDCT and NDCT image patches. The LDCT and corresponding NDCT image patches with a similarity over $s = 0.85$ are included into the training set. We call this as Patch Similarity Purification (PSP) strategy [52].

C. Training Denoising Transformers with NCCT Guidance

Here, we modify two image denoising transformers of SwinIR [40] and HAT [12] to exploit useful NCCT Guidance (NCG) for guided LDCT image denoising. For the networks without guidance, we only compute the similarity between the LDCT and corresponding NDCT image patches.

Modifying SwinIR [40] with our NCG for guided LDCT image denoising. Given an input feature of size $H \times W \times C$, the self-attention block in SwinIR first reshapes the feature into a size of $\frac{HW}{M^2} \times M^2 \times C$ by partitioning it into non-overlapping $M \times M$ local windows, where $\frac{HW}{M^2}$ is the number of local windows. Then, self-attention is performed separately for the feature map in each local window $X \in \mathbb{R}^{M^2 \times C}$ (Fig. 4 (a)). To incorporate the useful information of NCCT images for guided LDCT image denoising, we replace the self-attention in transformer layer of SwinIR by the cross-attention mechanism [8]. As shown in Fig. 4 (b), we extract local window features X from LDCT image patch and $Y \in \mathbb{R}^{M^2 \times C}$ from the corresponding NCCT image patch. Here, the query, key, and value matrices Q , K , and V are computed as:

$$Q = XP_Q, \quad K = YP_K, \quad V = XP_V, \quad (4)$$

where P_Q , P_K , and P_V are linear projection matrices that are shared across different local windows. Then we have Q , K , and V all of size $M^2 \times d$. The attention matrix is computed the same as that in self-attention:

$$\text{Attention}(Q, K, V) = \text{SoftMax}\left(\frac{QK^T}{\sqrt{d}} + B\right)V, \quad (5)$$

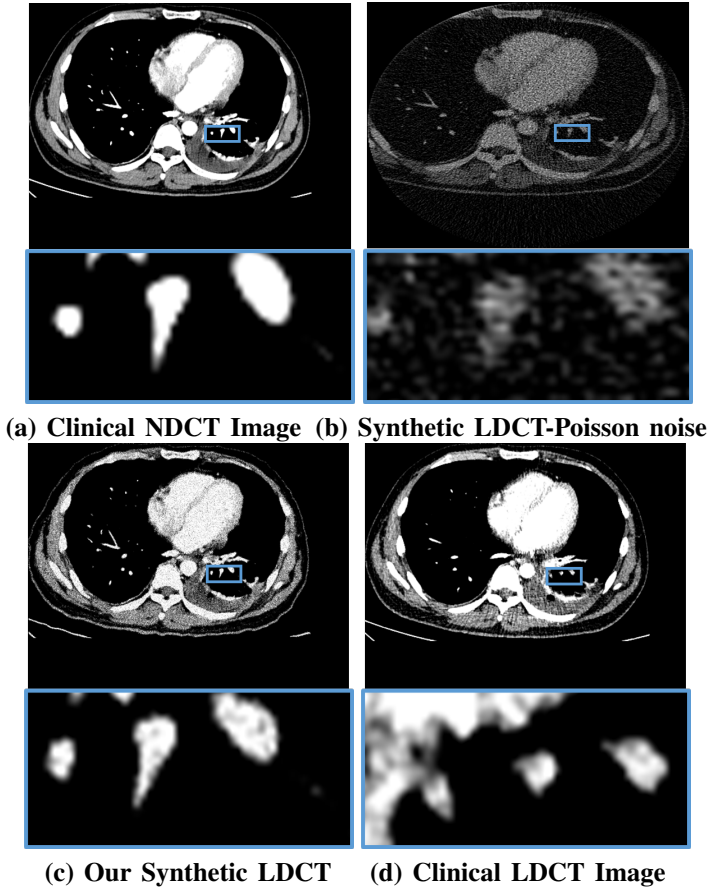


Figure 5. Synthetic LDCT images based on the Poisson noise adding to the sinogram data of the corresponding NDCT image v.s. our synthetic LDCT image. (a) NDCT image from real world. (b) Synthetic LDCT image by adding Poisson noise adding to the sinogram data of the corresponding NDCT image. (c) Our synthetic LDCT image. (d) Real-world LDCT image.

where B is the learnable relative positional encoding. For modified SwinIR, we use four RSTB layers with two Swin-Transformer layers in each RSTB layer.

Modifying HAT [12] with our NCG for guided LDCT image denoising. HAT combines channel attention [24] and window-based self-attention for feature learning. Here, we also replace the vanilla self-attention (Fig. 4 (a)) with cross-attention (Fig. 4 (b)) to utilize the NCCT images for useful guidance on LDCT image denoising. Similar to the modification on SwinIR, we extract local window features X and Y from the LDCT and NCCT image patches, respectively. We then transform X to the query/value matrices and transform Y to the key matrix. For modified HAT, we use four RHAG layers with two HAB blocks in each RHAG layer.

Loss function. We train different denoising transformers with a combination of Charbonnier loss function ℓ_C [7] and perceptual loss function ℓ_P [28], as follows:

$$\mathcal{L} = \ell_C + \lambda \ell_P, \quad (6)$$

where λ is a hyper-parameter to trade-off the two loss functions. Here, we simply set $\lambda = 1$.

IV. OUR DATASETS

A. Synthetic Dataset

Some studies [9] in the past synthesize the LDCT images by adding Poisson noise to the sinogram data of the NDCT ones. However, in the real world, there is not only noise between LDCT images and NDCT images, but also overall image shift and incomplete shape matching. Based on this, we introduce random displacement and elastic deformation [51] when synthesizing LDCT images. The synthesis of LDCT images can be divided into the following three steps.

Add random displacement. Firstly, for the randomly divided test set, training set, and validation set of normal dose CT images, we randomly shift the NDCT images of the divided training, validation, and test sets by $2 \sim 5$ pixels horizontally or vertically.

Add elastic deformation. Secondly, we introduce elastic deformation [51] to the image to simulate the structural distortion of low-dose CT images compared to normal-dose CT images in the real world. When adding elastic deformation, we set the control factor α as 25.

Add Gaussian noise. Thirdly, we add zero-mean Gaussian noise with a standard deviation of $\sigma = 40$ to generate synthetic LDCT images. For each triplets of LDCT, NDCT, and NCCT patches, we crop it into 64×64 patches.

From Fig. 5, we can see that compared to add Poisson noise to the sinogram data of the NDCT images, our simulated LDCT images not only simulate the noise of clinical LDCT images, but also simulate the structural distortions between LDCT images and NDCT images in the real world.

B. Clinical Dataset

1) *Existing Datasets and Our Motivations:* Common CT noise reduction datasets include: the AAPM-Mayo dataset [43], the NBIA/NCIA dataset [49], the Piglet dataset [66], the Data Science Bowl 2017 [66]. The first two datasets synthesize the LDCT images from adding Poisson noise to the sinogram data of the NDCT ones. The AAPM-Mayo dataset comprises 2,378 512×512 NDCT images and simulated LDCT images from 10 patients generated by adding Poisson noise in the sinogram domain of NDCT images [43]. In this dataset, the radiation dose from the LDCT images are approximately 25% of that from the NDCT images. The NBIA/NCIA dataset contains 7,015 NDCT images with diverse organ data [49]. However, the distribution of simulated noise is very different from the actual clinical noise. The Piglet dataset contains 850 pairs of LDCT and NDCT whole-body images, with four levels of noise by adjusting the tube current to 50%, 25%, 10%, and 5% of that used in capturing NDCT images [66]. The Data Science Bowl 2017 provides 850 low-dose CT images from high-risk patients, with no corresponding NDCT ones [66]. The two smaller datasets are appropriate for performance evaluation but unsuitable for training advanced networks. In summary, the existing CT noise reduction datasets face challenges of discrepancies between simulations and real-world scenarios, along with limited data volume. To address the challenges above, we have collected a large number of NCCT images

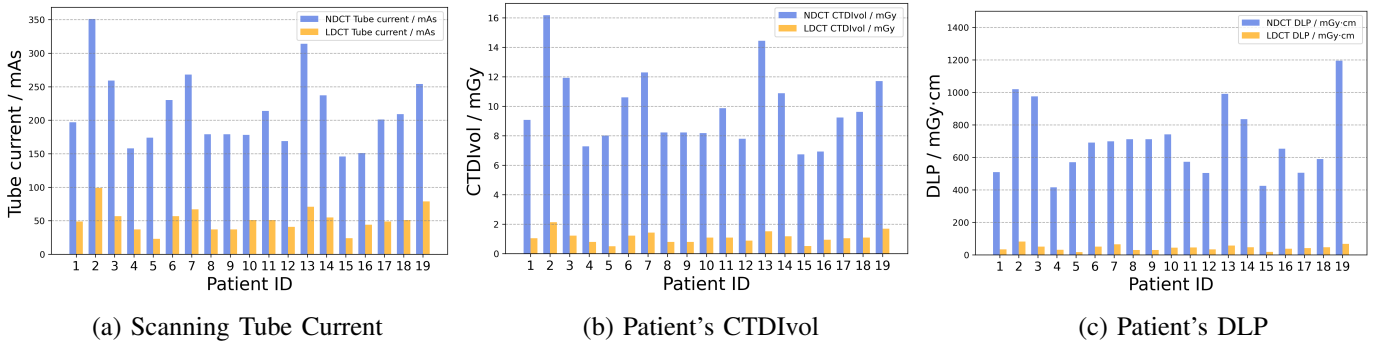


Figure 6. **Statistics of the clinical dataset.** (a) The tube current parameters during the patient scanning process. The normal dose tube voltage is 100 kVp, while the low dose is 80 kVp. The NCCT is the same as the normal dose. (b) Average CT DIvol values of the three scan phases for the patients. (c) Average DLP values of the three scan phases for the patients.

and matched LDCT and NDCT images from three-phase scans from clinical practice.

2) *Introduction of Our clinical dataset:* The NCCT images refer to the internal cross-sectional images of the human body reconstructed by a computer based on the attenuation degree of X-rays, which are obtained by passing X-ray beams through the body from different angles without injecting contrast agents. They are usually used for preliminary examinations. The LDCT and NDCT images are obtained from three-phase scanning, which is a special CT examination method involving three different stages of CT scanning after intravenous injection of contrast agents. The three phases are commonly referred to as the arterial phase, the venous phase or equilibrium phase, and the delayed phase. They further reveal the vascularization characteristics and enhanced lesion patterns, which helps more accurate diagnoses of disease.

Here we construct a new dataset scanned from 19 patients to provide large-scale real-world LDCT, NDCT and NCCT image triplets. The data collection for this study was approved by the Institutional Review Board of The First Affiliated Hospital of Xi’an Jiaotong University. All CT scans were performed in a 320-row spiral CT scanner uCT960+ from United Imaging Healthcare, with a rotation time of 0.5 s/rotation, a pitch of 0.9937, and a collimation width of 80 mm. The acquired raw data were transformed into the final CT images in the United Imaging Healthcare’s uInnovation-CT Explorer platform (R001). During the scanning process, the vascular monitoring scans employed contrast agent tracking technology, with the monitoring plane positioned at the descending aorta of rabbits and used a trigger threshold of 100 Hounsfield Units (HU). Once the threshold was reached, the scan was triggered with a delay time of 12 seconds. For the arterial phase, the normal-dose and low-dose scans were conducted at approximately 12.0 and 15.4 seconds, respectively. For the portal venous phase, the normal-dose and low-dose scans were conducted at approximately 28.0 and 31.4 seconds, respectively. For the delayed phase, the normal-dose and low-dose scans were conducted at approximately 40.0 and 43.4 seconds, respectively. Compared to NDCT images, NCCT images only lack the addition of contrast agent, while other aspects of the scanning protocol remain the same.

For each CT scan, we recorded the metrics of Volume CT Dose Index (CT DIvol) and Dose Length Product (DLP) [16] to measure the radiation dose. The Effective Dose (ED) is

calculated by $ED = DLP \times k$, where k is the radiation dose conversion factor usually set as 0.015 mSv/(mGy-cm) for the abdomen [29]. As shown in Fig. 6, with the decrease in scanning tube current, the CTDI and DLP decrease from the normal doses of 9.85 mGy and 701.09 mGy-cm to 1.10 mGy and 43.71 mGy-cm, though bringing a significant amount of noise and artifacts.

Finally, we collect 17,541 LDCT images and corresponding NDCT/NCCT of 512×512 abdominal CT images. In subsequent experiments, we cropped the black area without content, resulting in an image size of 392×512 .

V. EXPERIMENTS

In this section, we first introduce our experimental setting in §V-A. We further compare our methods with other denoising networks on our synthetic and real-world patient datasets in §V-B and §V-C, respectively. Finally, we study the hyperparameters of the proposed methods in §V-D.

A. Experimental Setting

1) *Implementation Details:* The modified SwinIR and HAT for LDCT image denoising are optimized by AdamW [42] with $\beta_1 = 0.9$ and $\beta_2 = 0.99$. The learning rate is initialized as 2×10^{-4} and dynamically adjusted using the MultiStepLR strategy. The batch size is set as 32 in all experiments. We train all LDCT image denoising networks on an NVIDIA RTX 3090 GPU with 24GB memory. The window size is $M = 8$.

2) *Evaluation Metrics:* Due to the misalignment between real-world LDCT and NDCT images, we employ feature-level metrics such as Fréchet Inception Distance (FID) [20], Kernel Inception Distance (KID) [4] and sFID [46] to objectively evaluate the distributional distance (in terms of diversity and visual quality) between denoised LDCT images and clean NDCT images from our clinical dataset.

B. Comparison on Synthetic LDCT Images

1) *Synthetic Dataset:* Similar to clinical dataset, we select 13,704 image triplets from 15 randomly selected patients as the training set, 1,032 LDCT images from one patient as the validation set, and 2,805 LDCT images from the rest 3 patients as the test set. For each LDCT, NDCT, or NCCT image from our training set, we crop it into 64×64 patches with a 32-pixel

Table I
RESULTS OF MODIFIED HAT [12] USING DIFFERENT SIMILARITY THRESHOLDS s IN OUR PTSP STRATEGY ON OUR SYNTHETIC DATASET. "NCG": NCCT IMAGE GUIDANCE.

Method	Thre. s	sFID↓	FID↓	KID↓
HAT+NCG+PTSP	70%	38.00	28.29	2.13
	80%	37.47	25.55	1.67
	90%	58.59	55.21	5.27

Table II
RESULTS OF HAT [12] USING DIFFERENT DISCRETIZATION INTERVALS $n = 2, 3, 4$ WHEN IMPLEMENTING OUR PTSP STRATEGY WITH NCCT IMAGE GUIDANCE IN OUR SYNTHETIC DATASET.

Threshold (T)	sFID↓	FID↓	KID×100↓
[0,32,256]	40.70	32.78	2.57
[0,64,256]	42.76	35.65	2.80
[0,128,256]	39.73	29.35	2.17
[0,170,256]	38.08	26.37	1.84
[0,192,256]	38.02	28.97	2.14
[0,85,170,256]	38.50	30.35	2.26
[0,64,128,256]	37.47	25.55	1.67
[0,32,64,128,256]	38.68	28.31	1.97
[0,64,128,192,256]	38.72	30.99	2.28

overlap to train the LDCT image denoising networks. In this way, our synthetic training set has total 970,737 triplets of LDCT, NDCT, and NCCT patches.

2) *Comparison Methods*: On one hand, we conducted ablation experiments based on the introduction of the PTSP strategy and cross-attention HAT. From the Table I and the Table II, the results indicate that the optimal denoising results are achieved when the similarity threshold is set to 80% and the segmentation interval is set to [0,64,128,256], which validates the effectiveness of our PTSP strategy and NCG guidance via cross-attention. On the other hand, we compare the modified HAT with eleven other noise reduction models.

3) *Objective Results*: From the Table III, we summarize the objective results on our synthetic dataset. One can see that trained with our PTSP strategy and the NCCT image guidance via cross-attention, the modified HAT outperforms its vanilla models and other comparison methods on LDCT image denoising. This validates the effectiveness of our PTSP strategy on filtering the training data and NCCT image guidance on the restoration [38] of image structure for LDCT image denoising.

C. Comparison on Real-World LDCT Images

1) *Comparison Methods*: To study the effectiveness of our PTSP strategy and NCCT image guidance, we compare SwinIR [40] and HAT [12] trained with or without our PTSP strategy on LDCT image denoising. Note that these methods using our PTSP need the incorporation of cross-attention to accommodate the NCCT image guidance. We also compare the modified SwinIR and HAT trained with our PTSP strategy with fifteen image denoising methods, which can be divided into five categories: 1) three LDCT image denoising methods of WGAN-VGG [65], RED-CNN [9], and CTformer [56]; 2) four image denoising methods of BM3D [13],

Table III
RESULTS OF THE COMPARISON METHODS ON OUR SYNTHETIC DATASET. WHEN USING THE PTSP STRATEGY, WE SET THE SIMILARITY THRESHOLD AS $s = 0.85$. THE NUMBER OF SEGMENTS IS SET AS $n = 3$. $\{T_i\}_{i=1}^n$ IS SET AS $\{0, 64, 128, 256\}$, AND THE WEIGHTS ARE SET AS $\{1, 0.7, 0\}$. "NCG": NCCT IMAGE GUIDANCE.

Method	sFID↓	FID↓	KID×100↓
RED-CNN [9]	42.52	32.35	2.51
DnCNN [68]	38.35	27.79	1.96
NAFNet [11]	41.57	36.60	2.97
CTformer [56]	55.73	68.10	7.01
WGAN-VGG [65]	108.40	106.05	9.52
NAC [60]	82.67	99.43	10.21
BM3D [13]	117.64	114.37	11.46
MLEFGN [15]	37.79	26.18	1.78
SKWGIF [53]	108.52	122.46	12.68
HAT [12]	38.05	27.08	1.84
+ PSP [52]	39.10	28.74	2.06
+ NCG + PTSP	37.47	25.55	1.67

Table IV
RESULTS OF THE COMPARISON METHODS ON OUR CLINICAL DATASET. WHEN USING THE PTSP STRATEGY, WE SET THE SIMILARITY THRESHOLD AS $s = 0.85$. THE NUMBER OF SEGMENTS IS SET AS $n = 3$. $\{T_i\}_{i=1}^n$ IS SET AS $\{0, 64, 128, 256\}$, AND THE WEIGHTS ARE SET AS $\{1, 0.7, 0\}$. "NCG": NCCT IMAGE GUIDANCE.

Method	sFID↓	FID↓	KID×100↓
RED-CNN [9]	84.79	38.16	2.10
DnCNN [68]	88.78	48.16	3.34
NAFNet [11]	106.49	74.88	6.14
CTformer [56]	209.20	72.74	7.19
WGAN-VGG [65]	133.04	72.22	3.81
NAC [60]	104.32	61.84	4.46
BM3D [13]	147.52	96.69	8.46
MLEFGN [15]	87.80	46.59	3.41
SKWGIF [53]	123.25	71.68	5.26
AIIR-1	110.55	96.86	9.42
AIIR-3	93.48	56.99	4.48
AIIR-5	86.52	46.27	3.34
KARL-9	107.88	57.14	3.57
SwinIR [40]	89.20	50.36	3.62
+ RMSE	86.74	47.87	3.41
+ PSP [52]	83.26	36.32	1.96
+ NCG + PTSP	81.11	32.29	1.42
HAT [12]	105.18	41.35	2.40
+ RMSE	81.59	38.00	2.12
+ PSP [52]	80.46	35.99	1.89
+ NCG + PTSP	80.34	34.44	1.70

DnCNN [68], Noise-As-Clean (NAC) [60], and NAF-Net [11]; 3) two baselines of SwinIR [40] and HAT [12]; 4) two guided image denoising methods of MLEFGN [15] and SKWGIF [53]; 5) four commercial algorithms of AIIR-1, AIIR-3, AIIR-5, and KARL9 provided by United Imaging Healthcare.

2) *Objective Results*: Here, we summarize the results of comparison methods on the test set of our clinical dataset. The results summarized in the Table IV show that, trained with our PTSP strategy and the cross-attention for the guidance of NCCT images, the modified SwinIR and HAT outperforms not only their vanilla models but also the other comparison methods on LDCT image denoising, in terms of the sFID, FID, and KID. Besides, trained with PSP strategy [52], SwinIR and HAT outperform the vanilla models, in terms of the sFID, FID, and KID. This indicates that introducing NCCT image guidance

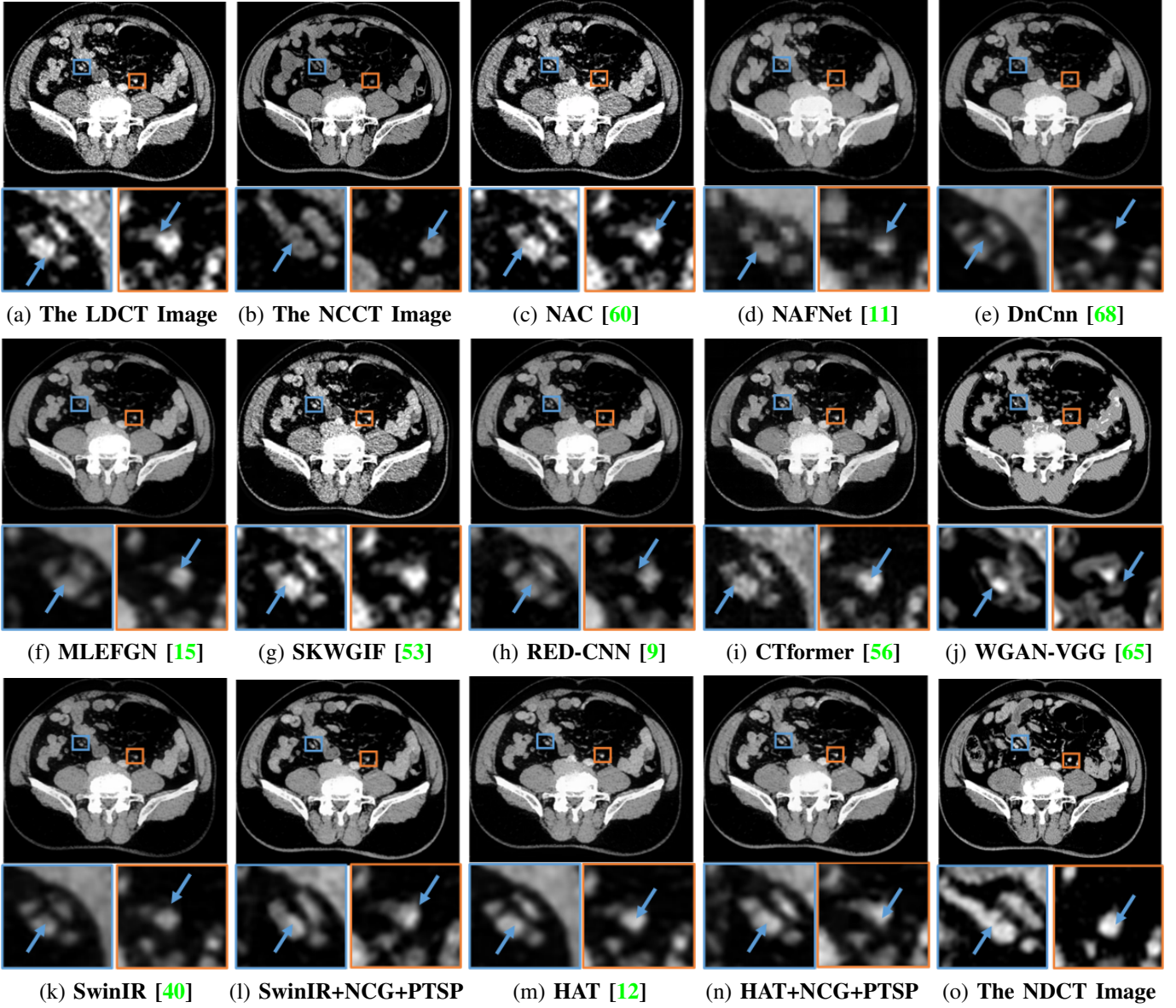


Figure 7. Comparison of visual quality by different denoising methods on one LDCT image from our clinical dataset.

and our PTSP strategy effectively improves the denoising effect of these methods.

3) *Visual Quality*: We compare the visual results of different image denoising methods on our clinical dataset. As shown in Fig. 7, the denoised image obtained by BM3D is over-smooth. The results of NAC and SKWGIF exhibit weak denoising effects. WGAN-VGG not only removes the noise but also generates visual artifacts, which would have significant side impacts on clinical diagnosis. The results of NAFNet, CTFormer, and DnCNN have obvious motion artifacts with some blurry areas. The results of RED-CNN and MLEFGN are close to the NDCT images from the overall visual effect, but suffer from distorted or blurry structure. Additionally, both the vanilla SwinIR and HAT exhibit slight motion artifacts and inconsistent details with the NDCT images. With our PTSP strategy, the modified SwinIR and HAT not only obtain results close to the NDCT images from the overall visual effect, but also well preserve the structure and details of the LDCT image.

D. Ablation Study

We conduct ablation studies to explore the working mechanism of our PTSP strategy and NCCT-guided cross-attention. Specifically, we assess: 1) the influence of different attention mechanisms to SwinIR and HAT on LDCT image denoising; 2) how do the number of segments n and the segmentation points $\{T_i\}_{i=0}^n$ affect the size of training set and the performance of modified SwinIR and HAT on guided LDCT image denoising; 3) the impact of different similarity thresholds s for guided LDCT image denoising.

1) **The influence of different attention mechanisms to SwinIR and HAT on LDCT image denoising.** The vanilla SwinIR and HAT use the self-attention (SA) mechanism. To incorporate the guidance from NCCT images, we modify SwinIR and HAT with our NCCT image guidance (NCG), which is implemented by replacing the SA with cross-attention (CA). To study its effectiveness, we compare the denoising results of SwinIR and HAT with or without our NCG on the

Table V
RESULTS OF SWINIR [40] AND HAT [12] USING SELF-ATTENTION (SA) OR CROSS-ATTENTION (CA) MECHANISM ON OUR CLINICAL DATASET. FOR SA MECHANISM, THE DATA SCREENING STRATEGY IS THE PSP STRATEGY [52] SINCE THERE IS NO NCCT IMAGE GUIDANCE.

Method	Attention	sFID↓	FID↓	KID↓
SwinIR+PSP [52]	SA	83.27	36.32	1.96
SwinIR+NCG+PTSP	CA	81.11	32.29	1.42
HAT+PSP [52]	SA	80.45	35.99	1.89
HAT+NCG+PTSP	CA	80.34	34.05	1.66

Table VI
RESULTS OF SWINIR [40] USING DIFFERENT DISCRETIZATION INTERVALS $n = 2, 3, 4$ WHEN IMPLEMENTING OUR PTSP STRATEGY WITH NCCT IMAGE GUIDANCE IN OUR CLINICAL DATASET.

Threshold (T)	sFID↓	FID↓	KID×100↓
[0,32,256]	84.66	36.04	1.86
[0,64,256]	84.10	35.63	1.71
[0,128,256]	88.47	42.54	2.49
[0,170,256]	90.69	37.47	1.54
[0,192,256]	86.06	37.30	1.74
[0,85,170,256]	81.50	32.26	1.36
[0,64,128,256]	81.11	32.29	1.42
[0,32,64,128,256]	83.04	33.65	1.56
[0,64,128,192,256]	81.87	33.04	1.39

training set selected by our PTSP strategy. From the Table V, one can see that after introducing NCCT image guidance (NCG), the modified SwinIR and HAT achieve boosted results on all metrics. For example, modified SwinIR achieves an improvement of sFID, FID, and KID by 2.6%, 11.1%, and 27.6%, respectively, while modified HAT achieves consistent improvements on all metrics by 0.11%, 5.4%, and 12.2%, respectively. This demonstrates that after introducing NCCT image guidance, the modified SwinIR and HAT not only effectively remove the realistic CT noise but also well preserve the LDCT image structure.

2) **How do the number of segments n and the segmentation points $\{T_i\}_{i=0}^n$ affect the size of training set and the performance of modified SwinIR and HAT on guided LDCT image denoising?** As mentioned in §III-B, our PTSP strategy requires to pre-define a discrete interval number n and a set of discrete interval segmentation points $\{T_i\}_{i=0}^n$. The purpose of our PTSP strategy is to select highly similar patch triplets from the aligned LDCT images, NDCT images, and NCCT images. The role of n and $\{T_i\}_{i=0}^n$ in this process is crucial, as they directly affect the quality of the training data as well as the denoising effect. Therefore, we set $n = 2, 3, 4$ with different sets of $\{T_i\}_{i=0}^n$ to explore the appropriate number of segmentation points and suitable segmentation intervals on the modified SwinIR and HAT using NCG guidance and our PTSP strategy. From the Table VI and the Table VII, we observe that modified SwinIR and HAT achieve the best FID and KID results when $n = 3$ and $\{T_i\}_{i=0}^3 = [0, 85, 170, 256]$ and achieve the best sFID results when $n = 3$ and $\{T_i\}_{i=0}^3 = [0, 64, 128, 256]$. However, the performance degrades when n is further increased to 4. Thus, we set $n = 3$ and $\{T_i\}_{i=0}^3 = [0, 64, 128, 256]$ in our PTSP strategy.

Table VII
RESULTS OF HAT [12] USING DIFFERENT DISCRETIZATION INTERVALS $n = 2, 3, 4$ WHEN IMPLEMENTING OUR PTSP STRATEGY WITH NCCT IMAGE GUIDANCE IN OUR CLINICAL DATASET.

Threshold (T)	sFID↓	FID↓	KID×100↓
[0,32,256]	82.14	35.86	1.70
[0,64,256]	83.17	34.48	1.59
[0,128,256]	88.41	39.57	2.14
[0,170,256]	85.68	38.10	1.59
[0,192,256]	85.04	37.64	1.87
[0,85,170,256]	81.73	33.83	1.47
[0,64,128,256]	80.34	34.05	1.66
[0,32,64,128,256]	82.76	35.79	1.66
[0,64,128,192,256]	85.41	41.57	2.28

Table VIII
RESULTS OF MODIFIED SWINIR [40] AND HAT [12] USING DIFFERENT SIMILARITY THRESHOLDS s IN OUR PTSP STRATEGY ON OUR CLINICAL DATASET. "NCG": NCCT IMAGE GUIDANCE.

Method	Thre. s	sFID↓	FID↓	KID↓
SwinIR+NCG+PTSP	80%	80.43	34.11	1.73
	85%	81.11	32.29	1.42
	90%	85.19	34.21	1.55
HAT+NCG+PTSP	80%	80.53	39.33	2.25
	85%	80.34	34.05	1.66
	90%	84.31	36.63	1.95

3) **The impact of different similarity thresholds s for guided LDCT image denoising.** The hyperparameter of similarity threshold s in our PTSP strategy mainly influences the size and quality of the training data. Higher threshold indicates better similarity quality but also decreases the number of patch triplets for network training. To choose a proper threshold for the modified SwinIR and HAT, we perform experiments on LDCT image denoising by setting $s = 0.80, 0.85,$ and 0.90 while keeping all other settings the same. From the Table VIII, it can be seen that when the similarity threshold s is set as 0.85, the modified SwinIR (SwinIR+NCG) achieves the best results on FID and KID, as well as the second best results on sFID (only 0.68 worse than that using the threshold of $s = 0.80$). The modified HAT (HAT+NCG) obtains the best results on sFID, FID, and KID when the similarity threshold is set as $s = 0.85$. These results demonstrate that smaller similarity threshold will bring more training data with stronger structure misalignment, resulting in worse denoising performance. A larger similarity threshold will lead to less training data, resulting in inadequate network training with degraded denoising performance. Therefore, it is proper to set the similarity threshold as $s = 0.85$ in our PTSP strategy.

VI. CONCLUSION

In this paper, by observing that the non-contrast CT (NCCT) images share similar context characteristics to the corresponding NDCT images from three-phase scanning, we proposed to incorporate useful information from clean NCCT images as useful guidance for real-world LDCT images denoising. We modified two image denoising transformers, *i.e.*, SwinIR and HAT, by replacing the vanilla self-attention mechanism with the cross-attention mechanism to accommodate the NCCT

image guidance. To alleviate the issue of spatial misalignment between real-world LDCT images and NDCT (or NCCT) images, we proposed a Patch Triplet Similarity Purification (PTSP) strategy to select highly similar triplets of LDCT, NDCT, and NCCT image patches for network training. Through extensive experiments on our clinical dataset, the modified SwinIR and HAT outperform fifteen comparison methods on LDCT image denoising. Extensive experiments on our clinical dataset demonstrate that the modified SwinIR and HAT outperform fifteen comparison methods on LDCT image denoising. They not only effectively remove the noise from LDCT images, but also preserve the original structure of LDCT images with the help of NCCT image guidance.

In the future, we will study the effectiveness of our NCCT image guidance and PTSP strategy on LDCT images with much lower radiation doses to pursue further radiation reduction. We hope that our work will be helpful for clinical applications.

VII. ACKNOWLEDGMENTS

The authors thank Liqi Xue for her invaluable contributions in helpful discussions and beautification of the figures.

REFERENCES

- [1] Alexander Kolesnikov Dirk Weissenborn Xiaohua Zhai Thomas Unterthiner Mostafa Dehghani Matthias Minderer Georg Heigold Sylvain Gelly Jakob Uszkoreit Neil Houlsby Alexey Dosovitskiy, Lucas Beyer. An image is worth 16x16 words: Transformers for image recognition at scale. *ICLR*, 2021.
- [2] Joshua Batson and Loic Royer. Noise2self: Blind denoising by self-supervision. In *International Conference on Machine Learning*, pages 524–533. PMLR, 2019.
- [3] Sutanu Bera and Prabir Kumar Biswas. Noise conscious training of non local neural network powered by self attentive spectral normalized markovian patch GAN for low dose CT denoising. *IEEE Transactions on Medical Imaging*, 40(12):3663–3673, 2021.
- [4] Mikołaj Bińkowski, Danica J Sutherland, Michael Arbel, and Arthur Gretton. Demystifying MMD GANs. In *Int. Conf. on Learning Representations (ICLR)*, pages 1–15, 2018.
- [5] Antoni Buades, Bartomeu Coll, and J-M Morel. A non-local algorithm for image denoising. In *2005 IEEE Computer Society Conference on Computer Vision and Pattern Recognition (CVPR'05)*, volume 2, pages 60–65. IEEE, 2005.
- [6] Adria Font Calvarons. Improved Noise2Noise denoising with limited data. In *Proceedings of the IEEE/CVF Conference on Computer Vision and Pattern Recognition*, pages 796–805, 2021.
- [7] Pierre Charbonnier, Laure Blanc-Feraud, Gilles Aubert, and Michel Barlaud. Two deterministic half-quadratic regularization algorithms for computed imaging. In *Proceedings of 1st International Conference on Image Processing*, volume 2, pages 168–172. IEEE, 1994.
- [8] Chun-Fu Richard Chen, Quanfu Fan, and Rameswar Panda. Crossvit: Cross-attention multi-scale vision transformer for image classification. In *Proceedings of the IEEE/CVF International Conference on Computer Vision*, pages 357–366, 2021.
- [9] Hu Chen, Yi Zhang, Mannudeep K Kalra, Feng Lin, Yang Chen, Peixi Liao, Jiliu Zhou, and Ge Wang. Low-dose CT with a residual encoder-decoder convolutional neural network. *IEEE Transactions on Medical Imaging*, 36(12):2524–2535, 2017.
- [10] Hu Chen, Yi Zhang, Weihua Zhang, Peixi Liao, Ke Li, Jiliu Zhou, and Ge Wang. Low-dose CT via convolutional neural network. *Biomedical optics express*, 8(2):679–694, 2017.
- [11] Liangyu Chen, Xiaojie Chu, Xiangyu Zhang, and Jian Sun. Simple baselines for image restoration. In *Proceedings of the European Conference on Computer Vision (ECCV)*, pages 17–33, 2022.
- [12] Xiangyu Chen, Xintao Wang, Wenlong Zhang, Xiangtao Kong, Yu Qiao, Jiantao Zhou, and Chao Dong. Hat: Hybrid attention transformer for image restoration. *arXiv:2309.05239*, 2023.
- [13] Kostadin Dabov, Alessandro Foi, Vladimir Katkovnik, and Karen Egiazarian. Image denoising by sparse 3-D transform-domain collaborative filtering. *IEEE Transactions on Image Processing*, 16(8):2080–2095, 2007.
- [14] Manoj Diwakar, Prabhishkek Singh, and Deepak Garg. Edge-guided filtering based CT image denoising using fractional order total variation. *Biomedical Signal Processing and Control*, 92:106072, 2024.
- [15] Faming Fang, Juncheng Li, Yiting Yuan, Tiejong Zeng, and Guixu Zhang. Multilevel edge features guided network for image denoising. *IEEE Transactions on Neural Networks and Learning Systems*, 32(9):3956–3970, 2020.
- [16] Lee W Goldman. Principles of CT: radiation dose and image quality. *Journal of Nuclear Medicine Technology*, 35(4):213–225, 2007.
- [17] Ian Goodfellow, Jean Pouget-Abadie, Mehdi Mirza, Bing Xu, David Warde-Farley, Sherjil Ozair, Aaron Courville, and Yoshua Bengio. Generative adversarial networks. *Communications of the ACM*, 63(11):139–144, 2020.
- [18] Kaiming He, Jian Sun, and Xiaoou Tang. Guided image filtering. *IEEE Transactions on Pattern Analysis and Machine Intelligence*, 35(6):1397–1409, 2012.
- [19] Allard Adriaan Hendriksen, Daniël Maria Pelt, and K Joost Batenburg. Noise2inverse: Self-supervised deep convolutional denoising for tomography. *IEEE Transactions on Computational Imaging*, 6:1320–1335, 2020.
- [20] Martin Heusel, Hubert Ramsauer, Thomas Unterthiner, Bernhard Nessler, and Sepp Hochreiter. GANs trained by a two time-scale update rule converge to a local nash equilibrium. *Advances in Neural Information Processing Systems*, 30, 2017.
- [21] Zhiwei Hong, Xiaocheng Fan, Tao Jiang, and Jianxing Feng. End-to-end unpaired image denoising with conditional adversarial networks. In *Proceedings of the AAAI Conference on Artificial Intelligence*, volume 34, pages 4140–4149, 2020.
- [22] Yingkun Hou and Dinggang Shen. Image denoising with morphology- and size-adaptive block-matching transform domain filtering. *EURASIP Journal on Image and Video Processing*, 2018:1–16, 2018.
- [23] Hedvig Hricak, David J Brenner, S James Adelstein, Donald P Frush, Eric J Hall, Roger W Howell, Cynthia H McCollough, Fred A Mettler, Mark S Pearce, Orhan H Suleiman, et al. Managing radiation use in medical imaging: A multifaceted challenge. *Radiology*, 258(3):889–905, 2011.
- [24] Jie Hu, Li Shen, and Gang Sun. Squeeze-and-excitation networks. In *Proceedings of the IEEE Conference on Computer Vision and Pattern Recognition*, pages 7132–7141, 2018.
- [25] Zhanli Hu, Changhui Jiang, Fengyi Sun, Qiyang Zhang, Yongshuai Ge, Yongfeng Yang, Xin Liu, Hairong Zheng, and Dong Liang. Artifact correction in low-dose dental CT imaging using wasserstein generative adversarial networks. *Medical Physics*, 46(4):1686–1696, 2019.
- [26] Binbin Huo, Xiaomin Chen, Zhiyong Xu, Dongdong He, and Jin Wang. Exposure frequency and radiation dose from CT examinations in Huaian. *Radiation Protection Dosimetry*, 200(4):396–402, 2024.
- [27] Guowei Jiang, Ting Luo, Haiyong Xu, Sheng Nie, Yang Song, and Zhouyan He. GDAFormer: Gradient-guided Dual Attention Transformer for low-dose CT image denoising. *Biomedical Signal Processing and Control*, 94:106260, 2024.
- [28] Justin Johnson, Alexandre Alahi, and Li Fei-Fei. Perceptual losses for real-time style transfer and super-resolution. In *Computer Vision—ECCV 2016: 14th European Conference, Amsterdam, The Netherlands, October 11–14, 2016, Proceedings, Part II 14*, pages 694–711. Springer, 2016.
- [29] Willi A Kalender. Dose in X-ray computed tomography. *Physics in Medicine & Biology*, 59(3):129, 2014.
- [30] Eunhee Kang, Won Chang, Jaejun Yoo, and Jong Chul Ye. Deep convolutional framelet denoising for low-dose CT via wavelet residual network. *IEEE Transactions on Medical Imaging*, 37(6):1358–1369, 2018.
- [31] Eunhee Kang, Hyun Jung Koo, Dong Hyun Yang, Joon Bum Seo, and Jong Chul Ye. Cycle-consistent adversarial denoising network for multiphase coronary CT angiography. *Medical Physics*, 46(2):550–562, 2019.
- [32] Eunhee Kang, Junhong Min, and Jong Chul Ye. A deep convolutional neural network using directional wavelets for low-dose X-ray CT reconstruction. *Medical Physics*, 44(10):e360–e375, 2017.
- [33] Orhan Hakki Karatas and Ebubekir Toy. Three-dimensional imaging techniques: A literature review. *European Journal of Dentistry*, 8(01):132–140, 2014.
- [34] Alexander Krull, Tim-Oliver Buchholz, and Florian Jug. Noise2void-learning denoising from single noisy images. In *Proceedings of the IEEE/CVF Conference on Computer Vision and Pattern Recognition*, pages 2129–2137, 2019.
- [35] KA Saneera Hemantha Kulathilake, Nor Aniza Abdullah, Aznul Qalid Md Sabri, and Khin Wee Lai. A review on deep learning approaches for low-dose computed tomography restoration. *Complex & Intelligent Systems*, 9(3):2713–2745, 2023.
- [36] Haoran Li, Xiaomin Yang, Sihan Yang, Daoyong Wang, and Gwanggil

- Jeon. Transformer with double enhancement for low-dose CT denoising. *IEEE Journal of Biomedical and Health Informatics*, 27(10):4660–4671, 2022.
- [37] Ming Li, Jiping Wang, Yang Chen, Yufei Tang, Zhongyi Wu, Yujin Qi, Haochuan Jiang, Jian Zheng, and Benjamin MW Tsui. Low-dose CT image synthesis for domain adaptation imaging using a generative adversarial network with noise encoding transfer learning. *IEEE Transactions on Medical Imaging*, 42(9):2616–2630, 2023.
- [38] Sanqian Li, Binjie Qin, Jing Xiao, Qiegen Liu, Yuhao Wang, and Dong Liang. Multi-channel and multi-model-based autoencoding prior for grayscale image restoration. *IEEE Transactions on Image Processing*, 29:142–156, 2020.
- [39] Zhengguo Li, Jinghong Zheng, Zijian Zhu, Wei Yao, and Shiqian Wu. Weighted guided image filtering. *IEEE Transactions on Image Processing*, 24(1):120–129, 2014.
- [40] Jingyun Liang, Jiezhong Cao, Guolei Sun, Kai Zhang, Luc Van Gool, and Radu Timofte. Swinir: Image restoration using swin transformer. In *Proceedings of the IEEE/CVF International Conference on Computer Vision*, pages 1833–1844, 2021.
- [41] Huabing Liu, Jiawei Huang, Dengqiang Jia, Qian Wang, Jun Xu, and Dinggang Shen. Transferring adult-like phase images for robust multi-view isointense infant brain segmentation. *IEEE Transactions on Medical Imaging*, 2024.
- [42] Ilya Loshchilov, Frank Hutter, et al. Fixing weight decay regularization in adam. *Proc. Int. Conf. Learn. Represent. (ICLR)*, pages 1–13, 2018.
- [43] Cynthia H McCollough, Adam C Bartley, Rickey E Carter, Baiyu Chen, Tammy A Drees, Phillip Edwards, David R Holmes III, Alice E Huang, Farhana Khan, Shuai Leng, et al. Low-dose CT for the detection and classification of metastatic liver lesions: Results of the 2016 low dose CT grand challenge. *Medical Physics*, 44(10):e339–e352, 2017.
- [44] Mingqiang Meng, Yongbo Wang, Manman Zhu, Xi Tao, Zerui Mao, Jingyi Liao, Zhaoying Bian, Dong Zeng, and Jianhua Ma. Ddt-net: Dose-agnostic dual-task transfer network for simultaneous low-dose CT denoising and simulation. *IEEE Journal of Biomedical and Health Informatics*, 28(6):3613–3625, 2024.
- [45] Xiangxi Meng, Kaicong Sun, Jun Xu, Xuming He, and Dinggang Shen. Multi-modal modality-masked diffusion network for brain MRI synthesis with random modality missing. *IEEE Transactions on Medical Imaging*, 2024.
- [46] Charlie Nash, Jacob Menick, Sander Dieleman, and Peter W Battaglia. Generating images with sparse representations. In *IEEE Int. Conf. Vis. Commun. Image Process.*, pages 7958–7968, 2021.
- [47] Chuang Niu, Mengzhou Li, Fenglei Fan, Weiwen Wu, Xiaodong Guo, Qing Lyu, and Ge Wang. Noise suppression with similarity-based self-supervised deep learning. *IEEE Transactions on Medical Imaging*, 42(6):1590–1602, 2022.
- [48] Saowapark Pooisiri, Anchali Krisanachinda, and Kitiwat Khamwan. Evaluation of patient radiation dose and risk of cancer from CT examinations. *Radiological Physics and Technology*, 17(1):176–185, 2024.
- [49] Fred Prior, Kirk Smith, Ashish Sharma, Justin Kirby, Lawrence Tarbox, Ken Clark, William Bennett, Tracy Nolan, and John Freymann. The public cancer radiology imaging collections of The Cancer Imaging Archive. *Scientific Data*, 4(1):1–7, 2017.
- [50] Siva P Raman, Mahadevappa Mahesh, Robert V Blasko, and Elliot K Fishman. CT scan parameters and radiation dose: Practical advice for radiologists. *Journal of the American College of Radiology*, 10(11):840–846, 2013.
- [51] P.Y. Simard, D. Steinkraus, and J.C. Platt. Best practices for convolutional neural networks applied to visual document analysis. In *Seventh International Conference on Document Analysis and Recognition, 2003. Proceedings.*, pages 958–963, 2003.
- [52] Zeya Song, Liqi Xue, Jun Xu, Baoping Zhang, Chao Jin, Jian Yang, and Changliang Zou. Real-world low-dose CT image denoising by patch similarity purification. *IEEE Transactions on Image Processing*, 34:196–208, 2025.
- [53] Zhonggui Sun, Bo Han, Jie Li, Jin Zhang, and Xinbo Gao. Weighted guided image filtering with steering kernel. *IEEE Transactions on Image Processing*, 29:500–508, 2019.
- [54] Chao Tang, Jie Li, Linyuan Wang, Ziheng Li, Lingyun Jiang, Ailong Cai, Wenkun Zhang, Ningning Liang, Lei Li, and Bin Yan. Unpaired low-dose CT denoising network based on cycle-consistent generative adversarial network with prior image information. *Computational and Mathematical Methods in Medicine*, 2019(1):8639825, 2019.
- [55] Anne Van der Werf, Ingeborg M Dekker, Martijn R Meijerink, Nicolette J Wierdsma, Marian AE de van der Schueren, and Jacqueline AE Langius. Skeletal muscle analyses: Agreement between non-contrast and contrast CT scan measurements of skeletal muscle area and mean muscle attenuation. *Clinical Physiology and Functional Imaging*, 38(3):366–372, 2018.
- [56] Dayang Wang, Fenglei Fan, Zhan Wu, Rui Liu, Fei Wang, and Hengyong Yu. Ctformer: convolution-free Token2Token dilated vision transformer for low-dose CT denoising. *Physics in Medicine & Biology*, 68(6):065012, 2023.
- [57] Dayang Wang, Zhan Wu, and Hengyong Yu. Ted-net: Convolution-free T2T vision transformer-based encoder-decoder dilation network for low-dose CT denoising. In *Machine Learning in Medical Imaging, Cham, Switzerland:Springer Int*, pages 416–425. Springer, 2021.
- [58] A Waswani, N Shazeer, N Parmar, J Uszkoreit, L Jones, A Gomez, L Kaiser, and I Polosukhin. Attention is all you need. In *NIPS*, 2017.
- [59] Jelmer M Wolterink, Tim Leiner, Max A Viergever, and Ivana Išgum. Generative adversarial networks for noise reduction in low-dose CT. *IEEE Transactions on Medical Imaging*, 36(12):2536–2545, 2017.
- [60] Jun Xu, Yuan Huang, Ming-Ming Cheng, Li Liu, Fan Zhu, Zhou Xu, and Ling Shao. Noisy-as-clean: Learning self-supervised denoising from corrupted image. *IEEE Transactions on Image Processing*, 29:9316–9329, 2020.
- [61] Jun Xu, Lei Zhang, and David Zhang. A trilateral weighted sparse coding scheme for real-world image denoising. In *Proceedings of the European Conference on Computer Vision (ECCV)*, pages 20–36, 2018.
- [62] Jun Xu, Lei Zhang, David Zhang, and Xiangchu Feng. Multi-channel weighted nuclear norm minimization for real color image denoising. In *Proceedings of the IEEE/CVF International Conference on Computer Vision*, pages 1096–1104, 2017.
- [63] Jun Xu, Lei Zhang, Wangmeng Zuo, David Zhang, and Xiangchu Feng. Patch group based nonlocal self-similarity prior learning for image denoising. In *Proceedings of the IEEE International Conference on Computer Vision*, pages 244–252, 2015.
- [64] Liutao Yang, Zhongnian Li, Rongjun Ge, Junyong Zhao, Haipeng Si, and Daoqiang Zhang. Low-dose CT denoising via sinogram inner-structure transformer. *IEEE Transactions on Medical Imaging*, 42(4):910–921, 2023.
- [65] Qingsong Yang, Pingkun Yan, Yanbo Zhang, Hengyong Yu, Yongyi Shi, Xuanqin Mou, Mannudeep K Kalra, Yi Zhang, Ling Sun, and Ge Wang. Low-dose CT image denoising using a generative adversarial network with wasserstein distance and perceptual loss. *IEEE Transactions on Medical Imaging*, 37(6):1348–1357, 2018.
- [66] Xin Yi and Paul Babyn. Sharpness-aware low-dose CT denoising using conditional generative adversarial network. *Journal of Digital Imaging*, 31:655–669, 2018.
- [67] Xiaohua Zhai, Avital Oliver, Alexander Kolesnikov, and Lucas Beyer. S4I: Self-supervised semi-supervised learning. In *Proceedings of the IEEE/CVF International Conference on Computer Vision*, pages 1476–1485, 2019.
- [68] Kai Zhang, Wangmeng Zuo, Yunjin Chen, Deyu Meng, and Lei Zhang. Beyond a gaussian denoiser: Residual learning of deep CNN for image denoising. *IEEE Transactions on Image Processing*, 26(7):3142–3155, 2017.
- [69] Tao Zhang, Ying Fu, and Jun Zhang. Guided hyperspectral image denoising with realistic data. *International Journal of Computer Vision*, 130(11):2885–2901, 2022.
- [70] Wenzhao Zhao, Qiegen Liu, Yisong Lv, and Binjie Qin. Texture variation adaptive image denoising with nonlocal PCA. *IEEE Transactions on Image Processing*, 28(11):5537–5551, 2019.
- [71] Jun-Yan Zhu, Taesung Park, Phillip Isola, and Alexei A Efros. Unpaired image-to-image translation using cycle-consistent adversarial networks. In *Proceedings of the IEEE International Conference on Computer Vision*, pages 2223–2232, 2017.
- [72] Yuan Zou and Yinyao Ma. Edgeformer: Edge-enhanced transformer for high-quality image deblurring. In *2023 IEEE International Conference on Multimedia and Expo (ICME)*, pages 504–509. IEEE, 2023.